remote sensing

MDPI

Article

A Real-Time Permittivity Estimation Method for Stepped-Frequency Ground-Penetrating Radar by Full-Waveform Inversion

Xu Li [1,2,3], Shengbo Ye [1,2,*], Qingyang Kong [1,2,3], Chenyang Song [1,2], Xiaojun Liu [1,2] and Guangyou Fang [1,2,3]

[1] Aerospace Information Research Institute, Chinese Academy of Sciences, Beijing 100190, China; lixu211@mails.ucas.ac.cn (X.L.); kongqingyang21@mails.ucas.ac.cn (Q.K.); songchenyang@aircas.ac.cn (C.S.); lxjdr@mail.ie.ac.cn (X.L.); gyfang@mail.ie.ac.cn (G.F.)
[2] Key Laboratory of Electromagnetic Radiation and Sensing Technology, Chinese Academy of Sciences, Beijing 100190, China
[3] School of Electronic, Electrical and Communication Engineering, University of Chinese Academy of Sciences, Beijing 100049, China
* Correspondence: yesb@aircas.ac.cn

Abstract: Ground-penetrating radar (GPR) has been widely used in estimating the permittivity of mediums. The radar echo amplitude method is an important method used by GPR in this estimation, the basic step of which is to deduce the magnitude of the permittivity according to the relationship between the reflection coefficient and the permittivity. Based on the basic principle of the radar echo amplitude method, this paper proposes a full-wave inversion real-time permittivity estimation method that can be used for stepped-frequency GPR (SFGPR), which offers high efficiency, accuracy, and generalization ability. The characteristics of this method are mainly reflected in the following four aspects: Using the SFGPR system and introducing a layered media detection model, we can complete waveform compensation optimization with high precision. The distance between the antenna and the surface of the reflective medium is extracted from the time domain waveform without manual measurement, avoiding human measurement errors. The inversion of the total reflection waveform at the required height works under the principle of an electromagnetic field, eliminating the need for repeated metal plate calibration experiments and improving work efficiency and waveform accuracy. In a continuous measurement line, the total reflection waveform inversion on each measurement point can be efficiently completed, and the change of permittivity on the measurement line can be obtained. To evaluate the feasibility of the proposed method, we performed experiments on a wall of known thickness, and the permittivity estimation was basically consistent with that of the dielectric probe, physical model calculation, and wall penetration. We also successfully applied this method to the dielectric property analysis of adobe samples. The results indicate that the proposed method can help grasp the condition of a measured medium, which can ensure the accuracy of detection and improve subsequent data processing efficiency.

Keywords: permittivity; ground-penetrating radar (GPR); total reflection waveform; inversion; reflection coefficient

Citation: Li, X.; Ye, S.; Kong, Q.; Song, C.; Liu, X.; Fang, G. A Real-Time Permittivity Estimation Method for Stepped-Frequency Ground-Penetrating Radar by Full-Waveform Inversion. *Remote Sens.* **2023**, *15*, 5188. https://doi.org/10.3390/rs15215188

Academic Editor: Roberto Orosei

Received: 29 September 2023
Revised: 26 October 2023
Accepted: 27 October 2023
Published: 31 October 2023

1. Introduction

Ground-penetrating radar (GPR) is an effective means of detecting underground targets and a key technology for nondestructive testing [1–3], the basic working principle of which is to transmit electromagnetic waves to an underground or target medium through the transmitting antenna. Subsequently, when the electromagnetic wave encounters different electrical media interfaces or geometric forms during the propagation process, part of the energy is reflected and received by the receiving antenna. The waveform of the reflected wave changes with the interface or geometry encountered during propagation; then, the information of the detection medium can be obtained through the analysis of the

reflected signal, and the detection target can be imaged [4–7]. GPR has evolved into a key geophysical method for detecting near-surface environments, and its reflection measurements are commonly used as imaging tools in archaeological, engineering, environmental, and geological applications [8,9]. Conventional GPR is mostly ground-coupled radar; that is, the radar is in direct contact with the ground, and personnel need to follow the radar for real-time detection. However, for large-scale shallow detection of areas with large terrain fluctuations, or dangerous areas such as minefields, remote and harsh conditions limit the range of human-assisted surveying activities, so GPR cannot meet the direct coupling of antennas and the ground, rendering it powerless [10–12]. Therefore, in some application scenarios, it is necessary to develop an air-coupled GPR system.

In the past, most mainstream commercial GPRs used the time-domain pulse system, but owing to the large instantaneous bandwidth of the time-domain pulse system, the overall performance requirements of the hardware system were high. Moreover, to achieve such a large bandwidth, only equivalent sampling technology could be used, resulting in the introduction of time jitter, which affected the stability of the signal. With the development of microwave technology, large-scale integration technology, digital signal processing technology, and frequency synthesis technology, the advantages of stepper frequency technology have begun to emerge. Compared with time-domain pulsed GPR, stepped-frequency GPR (SFGPR) has the following advantages: an ultra-wide bandwidth, a low noise floor, and a high dynamic range, in addition to high average transmission power and the ability to directly store frequency domain signals, which is convenient for subsequent window processing and the application of some focusing algorithms. Additionally, different frequency attenuation characteristics can be used for media analysis [13]. With the improvement of the hardware level, the emergence of new signal processing methods, and the reduced price of vector network analyzers (VNA), more researchers began SFGPR research based on vector network analyzers. In 1989, Harmran first used VNA to build an SFGPR system, which was successfully applied to the detection of ice thickness [14]. As an ultra-wideband radar system, the antenna plays an important role in the performance of the entire system [15]. The ultra-wideband antenna produces dispersion, waveform tailing, multiple reflections, and other effects in the system, which widen the transmitted signal and reduce the resolution of the radar. Scholars worldwide have carried out studies to reduce the influence of antennas in GPR, such as designing antennas with better dispersion characteristics, but this method is costly and difficult in terms of design. Adding resistance at the end of the antenna can solve the tailing problem, but this approach reduces the antenna radiation efficiency. A series of digital processing methods have also been proposed, but the actual effect is insignificant. Lambot et al. proposed a layered media model of GPR under far-field conditions, which can complete the compensation of the antenna effect, and they proved through experiments that the resolution of GPR could be improved after compensation for the antenna effect [16–20].

Most natural materials on Earth are nonmagnetic; that is, $\mu_r = \mu/\mu_0 = 1$, where $\mu_0 = 4\pi \times 10^{-7}$ H/m is the magnetic permeability of free space. This means that for GPR, changes in the permittivity (ε) contribute the most to reflections. The propagation speed of the electromagnetic wave of the GPR in the medium is related to the permittivity of the medium, and it is no longer the propagation speed of free space; that is, $v_r = \frac{c}{\sqrt{\varepsilon_r}}$, where c is the propagation speed of electromagnetic waves in free space, and ε_r is the relative permittivity of the medium. The permittivity reflects the response ability of the medium to electromagnetic waves, and the different permittivity levels of the medium affect the propagation characteristics of radar electromagnetic waves. Therefore, an in-depth understanding of the permittivity of the medium can not only improve the accuracy of radar detection and measurement but also expand the application of radar technology in many fields, providing strong support for scientific research and engineering practice [21,22]. The traditional measurement method for the characteristics of the dielectric material includes the coring method—that is, drilling the core sample from the tested material and analyzing the characteristics of the core sample based on laboratory conditions. However, this

traditional method has great drawbacks; namely, it destroys the original structure of the dielectric material, the measurement cost is high, the efficiency is low, and long-term repeated measurement is not allowed. The electromagnetic exploration method represented by GPR technology can effectively solve these issues, and GPR can achieve nondestructive testing. Scholars worldwide have studied many media characteristics analysis methods based on GPR technology [23]. One of the more common methods for estimating permittivity is the common central point method point method, which uses a common center to analyze velocity. The midpoint or source position remains motionless, constantly changing the distance between the two antennas and recording the two-way travel time of the reflected wave. Even so, this method has a large error and is unreliable for near-surface characterization [24]. Based on the forward model of radar electromagnetic waves, it is a relatively rigorous GPR data analysis method to invert the dielectric characteristics of the medium. The basic principle is to calculate the radar echo through the forward simulation of radar waves. Then, the echo can be compared with the measured echoes to verify the correctness of the parameter settings of the forward model and determine whether the fitting of the two meets the accuracy requirements. However, the adjustment of the model parameters by this method is carried out manually, and the process is cumbersome, subjective, and arbitrary. In 2014, Sebastian et al. developed a full waveform inversion (FWI) scheme to estimate the permittivity and conductivity values by analyzing the reflected waves in the ground GPR data, but this laborious method requires continuous parameter optimization during the inversion process [25]. The radar echo amplitude method is a mature, widely used dielectric constant estimation method based on the reflection principle of electromagnetic waves; by analyzing the amplitude change of echo signals, one can estimate the permittivity of the medium. This method takes advantage of the relationship between the reflection coefficient and the permittivity to estimate the characteristics of the medium. In specific cases, total reflection echoes are usually generated by reflections from highly reflective surfaces such as metal plates [26]. Moreover, general radar systems need to use metal plates in the field to complete calibration procedures, so only single-point tests can be completed in the area of interest, and it is difficult to obtain changes in dielectric characteristics on a continuous measurement line [27].

Full waveform inversion (FWI) is one of the current research hotspots in the field of exploration geophysics. FWI can be described as a data fitting process based on seismic full-wave field simulation, which uses full-waveform information from seismic records. Full waveform inversion leverages all the information contained in the data and employs a high-resolution forward model, resulting in a higher resolution image. At present, FWI is quite mature enough to apply prototypes to 3D real-world datasets [28]. In 2014, F. Watson and W. Lionheart used SVD as an analysis tool in GPR full-wave inversion to help under-stand what a given acquisition system can image [29]. In 2019, Klotzsche, Anja et al, using crosshole GPR full-waveform inversion to visualize a soil aquifer system with variable saturation in critical regions, estimated four effective source wavelets with different source wavelets during inversion depending on the transmitter and receiver present in the saturated and/or unsaturated regions. Experiments have shown that this method can be used for imaging over the entire depth range starting from critical regions and can be applied to a wide range of applications [30]. Full waveform inversion is often used to estimate the geophysical parameters of recorded waveforms (observations) and is often expressed as a least squares optimization problem, but least squares FWI has a cycle jump problem. In 2022, SLEF da Silva et al. introduced a new Wasserstein metric within the framework of optimal transport (OT) for FWI analysis, which is based on the q-statistic and effectively reduces cycle skipping [31]. The characteristic analysis based on FWI ground penetrating radar has a wide application prospect and great research significance.

In this article, we (1) extend the GPR echo amplitude method to analyze the permittivity of the medium; (2) include a stepped-frequency air-coupled GPR system built by a single-horn antenna and VNA and then introduce a layered media detection model to filter out the direct coupling wave and correction time zero point of the system; (3) extract the

height between the antenna and the reflective surface of the medium from the processed time domain signal and then invert the total reflection waveform at the corresponding height according to the electromagnetic field theory; and (4) demonstrate the change law of permittivity on a measuring line and compare the estimated permittivity obtained with the average permittivity estimated by the dielectric probe and the physical quantity of the dielectric model.

The main innovations of this paper are as follows.

1. The direct wave and correction time zero can be removed by obtaining the parameter characteristics of the system, which has little impact on the echo signal of the target.
2. The distance between the radar and the reflective surface of the medium is obtained from the time domain signal of the radar, which avoids the error caused by human measurement.
3. The total reflected echo signal at this distance can be obtained by inversion using the system parameters and radar range, without the need to carry out repeated metal plate calibration experiments at the experimental site, which improves the efficiency of work.
4. Our proposed method can realize large-scale real-time permittivity measurement on a continuous measurement line.

The organization of this paper is as follows: Section 2 details the theory and workflow of the SFGPR system and permittivity estimation method, Section 3 presents the experimental results, Section 4 discusses the experimental results, and Section 5 summarizes the article.

2. Theory and Methodology

The workflow of this methodology, which consists of four parts, is summarized in Figure 1.

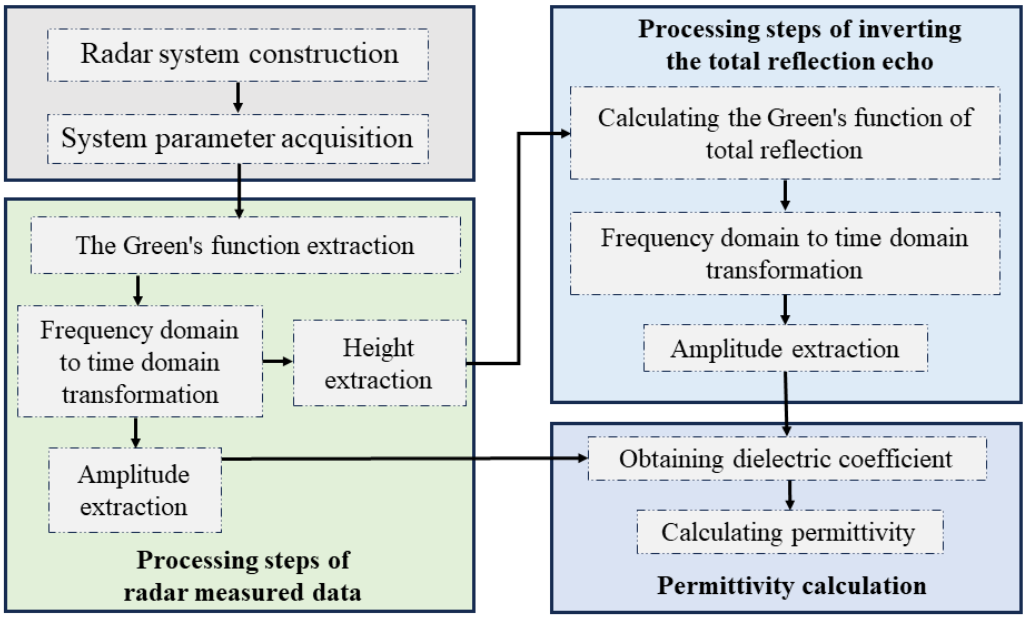

Figure 1. Scheme illustrating the processing workflow of the calculation for permittivity.

We introduce this method in detail following the workflow in Figure 1.

2.1. Introduction to Radar Systems

Vector network analyzers typically reflect the effect of the antenna by measuring the scattering coefficient S-parameter, which includes four modes, S11, S12, S21 and S22. The parameter S11 and S22 represent the amount of signal reflected from one port of the

device under test. For the purpose of reducing system cost and system weight, we use an antenna connected to a port to implement transmit and receive functions, and the measured parameters can be S11 or S22. In this system, we chose to collect S11 parameters. Because the horn antenna has strong directivity and wide impedance bandwidth [32], and the vector network analyzer module can work in S11 mode, an ultra-wideband doublespine horn antenna and VNA module were used to build a single-antenna SFGPR system. A horn antenna realizes the sharing of the transceiver and receiver and also reduces costs. The antenna operates in the frequency band of 1–6 GHz. The operating frequency band of the VNA is the same, containing a total of 201 frequency points, and the transmission power is zero dBm. Moreover, the entire radar system is equipped with a remote control rail module to present an air-coupled operating mode.

2.1.1. Radar System Modeling

According to the electromagnetic field theory, we can obtain the expression of the electric field generated in the x-direction after the electromagnetic wave radiated by the electric dipole in the x-direction has been reflected by the plane-layered medium [18,19].

$$E_{xx} = \frac{Il}{8\pi}\int_0^{\infty} G(k_\rho,\rho)\cdot k_\rho \cdot dk_\rho, \tag{1}$$

$$G(k_\rho,\rho) = \begin{bmatrix} J_0(k_\rho\cdot\rho)\left(\frac{k_{0z}}{j\omega\varepsilon_0}\tilde{R}^{TM} - \frac{j\omega\mu_0}{k_{0z}}\tilde{R}^{TE}\right) - \\ \cos(2\varphi)J_2(k_\rho\cdot\rho)\left(\frac{k_{0z}}{j\omega\varepsilon_0}\tilde{R}^{TM} + \frac{j\omega\mu_0}{k_{0z}}\tilde{R}^{TE}\right) \end{bmatrix}\cdot e^{-jk_{0z}(2d+z)}, \tag{2}$$

where $J_0(\cdot)$ represents the first class of $0-th$ order Bezier functions;$J_2(\cdot)$ represents the first class of second order Bezier functions; ρ represents the projection of the distance between the receiving point (x,y,z) and source point $(0,0,0)$ in the xoy plane; k is the wavenumber; $k_{0z} = \sqrt{k_0^2 - k_\rho^2}$; $k_\rho = x + jy$; $k_0^2 = \omega^2\varepsilon_0\mu_0$; ε_0 and μ_0 are the permittivity and permeability in air, respectively; $\tilde{R}^{TM}$ and $\tilde{R}^{TE}$ represent the global reflectance coefficients of TM waves and TE waves, respectively; $\omega = 2\pi f$; f is the frequency of the electromagnetic wave; $\cos(\cdot)$ represents the cosine function; and φ denotes the angle between the projection of the line between the field point and the source point in the xoy plane and the x-axis direction. j is the imaginary unit. The location relationship between the source point and the observation point are shown in Figure 2.

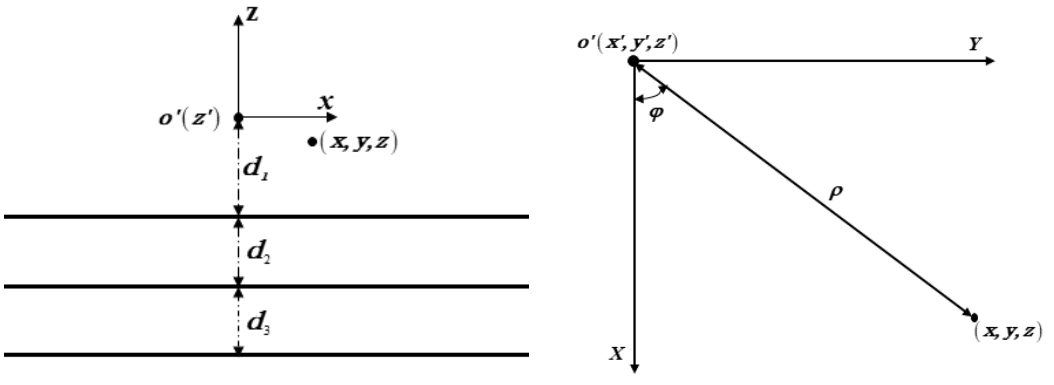

(**a**) (**b**)

Figure 2. The location relationship between the source point and the observation point: (**a**) XZ-plane position relationship. (**b**) XY-plane position relationship.

Since this system adopts the transceiver antenna multiplexing mode, the source point and the field point coincide; at this time $\rho = 0$, and Green's function can be simplified to

$$G_{xx} = \frac{Il}{8\pi} \int_0^\infty \left(\frac{k_{0z}}{j\omega\varepsilon_0} \tilde{R}^{TM} - \frac{j\omega\mu_0}{k_{0z}} \tilde{R}^{TE} \right) \cdot e^{-j2k_{0z}d_1} k_\rho dk_\rho. \tag{3}$$

The integral form of Equation (3) is the Sommerfeld integral, and we use the idea of deformed path integration (DPI) to calculate the Sommerfeld integral [33]. At this point, the contribution of the Bezier function disappears, and the exponential term in the integrable function produces violent oscillations. To reduce the oscillation behavior of the integrable function, we can find an integral path so that the phase of the exponential term remains unchanged over the entire integral path. Transforming the integral path into a point that is not in the first quadrant does not result in increasing the integral function drastically. Therefore, the reflected electric field at different distances (d_1) between the radar and the surface of the reflective medium can be obtained according to Equation (3), expressed as the zero-bias Green's function, $G_{xx}^0(\omega)$, when the source point coincides with the receiving field point.

Using the system function of the far-field radiation model for layered media detection applications proposed by Lambot [17], as shown in Figure 3, we locate the target in the far-field region of the antenna, and multiple reflections between the antenna and the target are considered. In the far-field region, assuming that the electric field measured locally by the antenna tends to be a plane wave, we can model the radar in a single-station configuration by a linear system with a frequency-dependent transfer function [17].

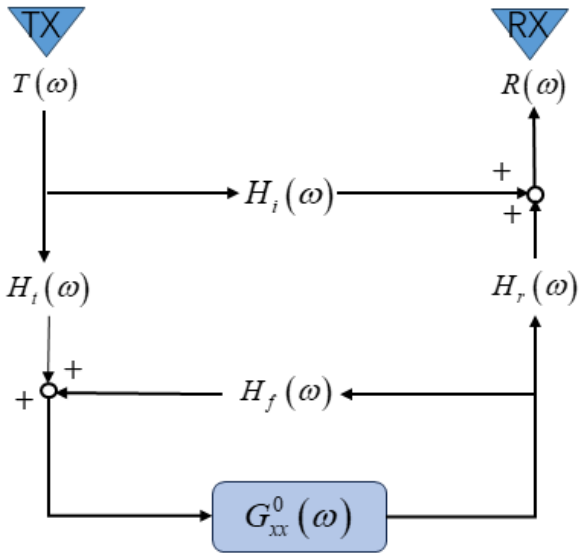

Figure 3. VNA–antenna multilayer media detection far-field radiation system function.

Simplifying Figure 3, the received signal of the radar can be denoted as [16,18–20]

$$S_{11}(\omega) = \frac{R(\omega)}{T(\omega)} = H_i(\omega) + \frac{H(\omega)G_{xx}^0(\omega)}{1 - H_f(\omega)G_{xx}^0(\omega)}, \tag{4}$$

$$H(\omega) = H_r(\omega)H_t(\omega), \tag{5}$$

where $R(\omega)$ represents the received signal, $T(\omega)$ represents the transmitted signal, $H_t(\omega)$ represents the transmission function of the transmitting antenna, $H_r(\omega)$ represents the reflection of the signal at the antenna port again after being transmitted by the medium, $H_i(\omega)$ represents reflections caused by other factors (the impedance mismatch between the VNA calibration plane and the antenna feed point, the impedance gradient inside the

antenna, and the impedance mutation between the antenna aperture plane and the free space), and $G^0_{xx}(\omega)$ represents the reflected electric field in the direction of the electric dipole per unit intensity in the layered medium.

To obtain the echo signal of the radar, we do not need to find the transmit transfer function $H_t(\omega)$ and the receive transfer function $H_r(\omega)$ separately; we only need to obtain their product, $H(\omega)$, so three unknowns are required in the above parameter model: $H_i(\omega)$, $H_f(\omega)$, $H(\omega)$. Thus, we need at least three different equations to obtain a solution. In the subsequent inversion process, the system parameters are directly called without recalculation, so the calculation cost of this part could be negligible.

2.1.2. Radar System Model Solving and Validation

To obtain the parameters of the radar system model and verify the accuracy of the above model, we had to perform calibration experiments. The equation was obtained by measuring $S_{11}(\omega)$ at different distances in front of a large enough metal plate by placing the antenna. The n-th equation can be denoted as

$$S_{11,n} = H_i + S_{11,n} \cdot G^0_{xx,n} \cdot H_f + G^0_{xx,n} \cdot \left(H - H_i \cdot H_f\right), \tag{6}$$

where $S_{11,n}$ represents the data measured by the radar at the n-th time, and $G^0_{xx,n}$ represents the Green's function calculated at the n-th altitude calculated by Equation (3). Since the radar is approximate modeling, to make the parameters of the solved radar model independent of the measurement distance, we made N measurements, where $N \geq 3$. These equations can be represented with a matrix as

$$y = Ex, \tag{7}$$

where

$$y = [S_{11,1} \cdots S_{11,m} \cdots S_{11,N}]^T, \tag{8}$$

$$E = \begin{bmatrix} 1 & S_{11,1}G^0_{xx,1} & G^0_{xx,1} \\ \vdots & \vdots & \vdots \\ 1 & S_{11,m}G^0_{xx,m} & G^0_{xx,m} \\ \vdots & \vdots & \vdots \\ 1 & S_{11,N}G^0_{xx,N} & G^0_{xx,N} \end{bmatrix}, \tag{9}$$

$$x = \begin{bmatrix} H_i \\ H_f \\ H - H_i H_f \end{bmatrix}. \tag{10}$$

Solving Equation (6) using the least squares criterion yielded the following form of solution:

$$x = \left(E^H E\right)^{-1} E^H y, \tag{11}$$

where the superscript ^{H} indicates conjugate transpose.

The antenna was placed within a range of 0.50–0.70 m in front of the metal plate for 21 measurements, and the distance step value was 0.01 m. The time-domain waveform at a distance of 0.52 m is shown in Figure 4. Observing Figure 4, we found that the waveform before 2.5 ns was the direct wave of the system and the reflection of the antenna mouth surface. Near 5.5 ns was the reflected signal of the metal plate received by the antenna. After 6 ns, we observed some oscillation signals, which were the waveform tailing of the reflected signal and the multiple reflections of the metal plate.

We substituted 21 sets of calibrated measured frequency domain echoes into the equation system, and we could obtain the amplitude and phase of the system parameters $H_i(\omega)$, $H_f(\omega)$, and $H(\omega)$ in the frequency domain, as shown in Figure 5.

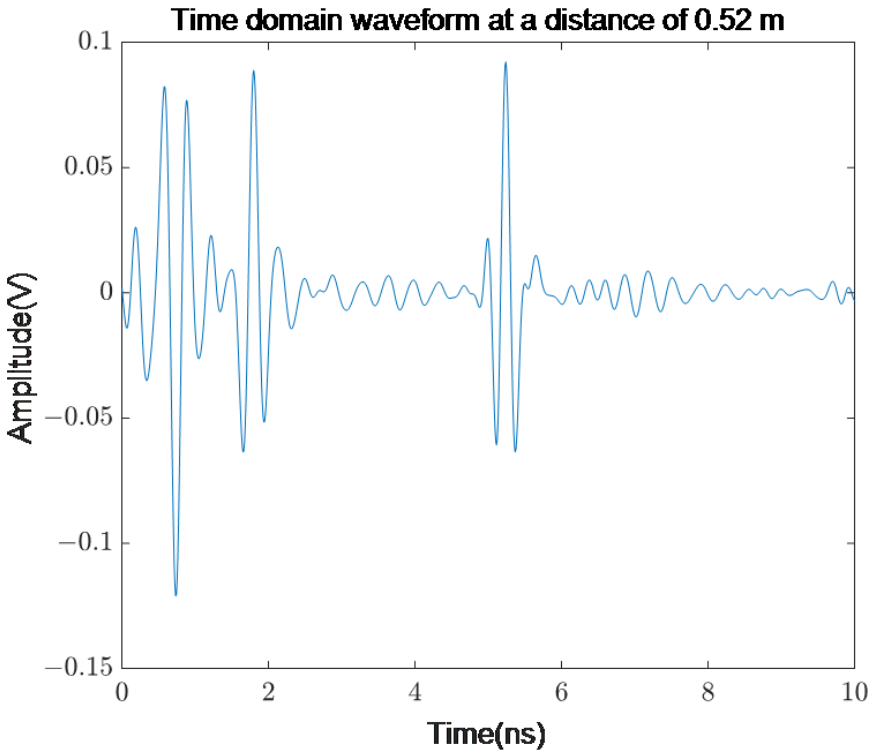

Figure 4. Measured waveform of the metal plate at 0.52 m.

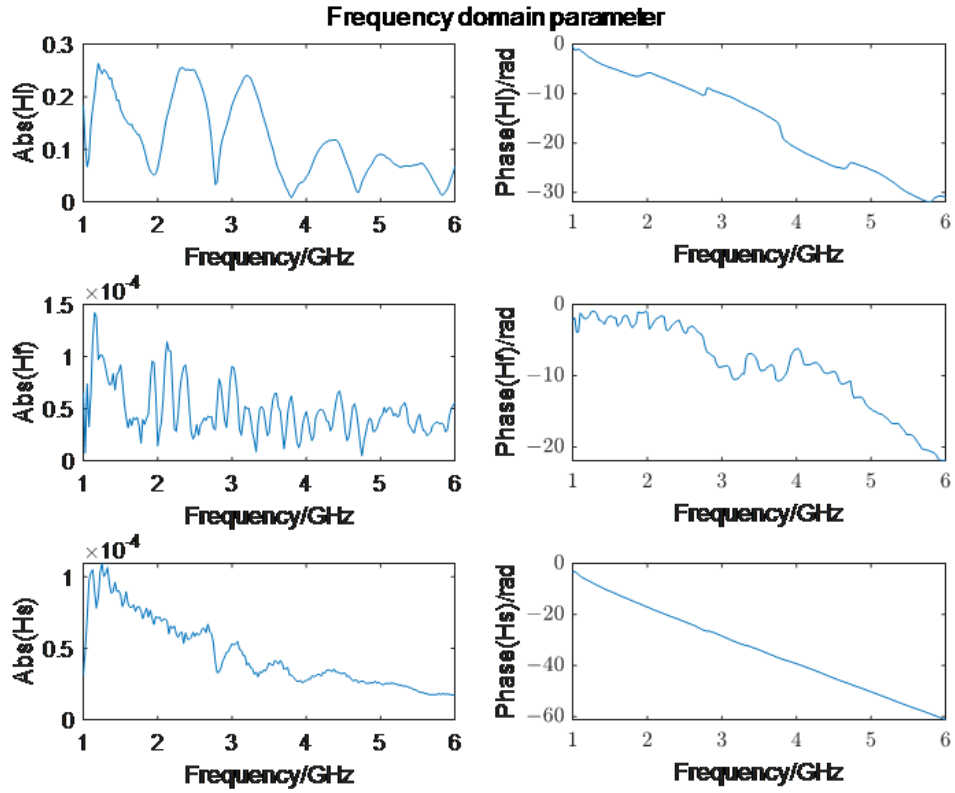

Figure 5. System frequency domain parameters.

In the antenna model, the effect of the antenna was only related to the frequency, the original waveform of the antenna could be converted into an equivalent zero-bias Green's function $G^0_{xx,r}$, and the extraction of the Green's function from the signal expression could

achieve the effect of effectively removing the direct wave and compensating for the zero point of time. According to Equation (4), the extraction formula of Green's function was as follows:

$$G^0_{xx,r}(\omega) = \frac{S_{11,r}(\omega) - H_i(\omega)}{H(\omega) + H_f(\omega)(S_{11,r}(\omega) - H_i(\omega))}. \quad (12)$$

The Green's function was extracted from the calibration waveform shown in Figure 4 to obtain its time domain waveform, which is shown by the red dashed line in Figure 6.

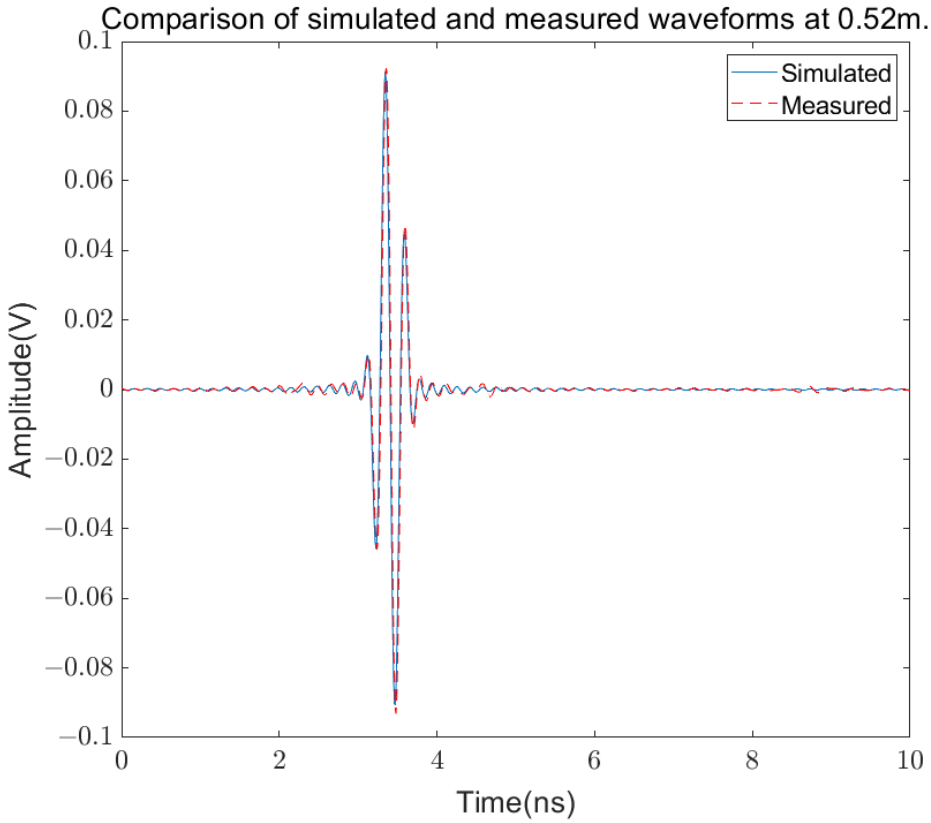

Figure 6. Comparison of simulated and measured waveforms at 0.52 m.

The red dashed line in Figure 6 shows the waveform of the reflected signal of the metal plate at 0.52 m after removing the direct wave and compensating for the zero point of time. After processing, the propagation time of the signal in the antenna was also naturally compensated, and the waveform moved forward. The red dashed line shows that the two-way time of the radar signal was 3.48 ns, which translates to a distance of 0.522 m between the antenna and the metal plate, consistent with the actual distance. At the same time, the reflected waves of the metal plate could be seen more clearly, accurately reflecting the characteristics of the reflected target.The solid blue line in Figure 6 shows the simulated Green's function at this distance calculated with Equation (3). Figure 6 shows that the actual reflected Green's function is essentially the same as the simulated Green's function, with a relative root mean square error of 1.63%.

At 0.46 m beyond the calibration distance of the antenna, the measured data and the simulation data were compared as shown in Figure 7. It can be seen from Figure 7 that the simulated waveform and the measured waveform had a high degree of agreement and that the relative root mean square error of the two was 0.24%, proving that the model has high accuracy and generalization ability.

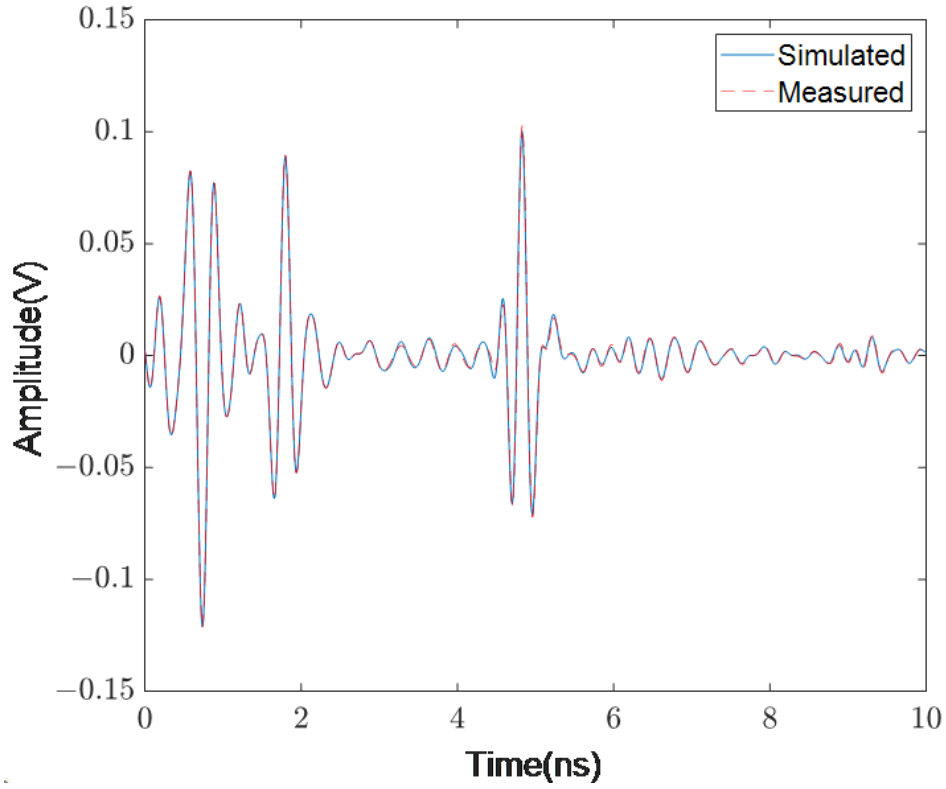

Figure 7. Comparison between measured waveform and simulated waveform at 0.46 m.

2.2. Introduction to the Method

The radar echo amplitude method is a method of estimating the permittivity of an electromagnetic wave by measuring the propagation and reflection of electromagnetic waves in the medium. The signal reflected from the surface of the dielectric to the receiving antenna is related to the reflectivity of the dielectric material and closely related to the permittivity value. The reflectance coefficient (γ) from material 1 to material 2 is defined as [21]

$$\gamma = \frac{\sqrt{\varepsilon_2} - \sqrt{\varepsilon_1}}{\sqrt{\varepsilon_2} + \sqrt{\varepsilon_1}}, \tag{13}$$

where ε_1 is the permittivity of material 1, and ε_2 is the permittivity of material 2. In the air-reflective surface (the surface of material 2) double-layer detection model, the permittivity of air defaults to 1, so we can intuitively calculate the permittivity of material 2. The reflectivity mentioned above is also defined as the peak ratio of the signal (i.e., that is, the ratio of the reflected echo amplitude on the surface of the medium to the total reflected echo amplitude), so the most critical step of the method is to obtain the time domain waveform of the two signals. The following describes the processing methods and processes of the two echoes.

2.2.1. Measured Data Processing

The established radar system was used to collect the frequency-domain-reflected echo signal (S_{11}^s) on the surface of the measured medium, and the system parameters obtained in Section 2.1 were substituted into Equation (12) to extract the Green's function of the measured echo signal (i.e., to remove clutter such as direct coupling waves and multiple reflections, and to correct the time zero point of the waveform). The Green's function of the measured signal can be denoted as $G_{xx,s}^0(\omega)$. $G_{xx,s}^0(\omega)$ in the above equation serves as the frequency-domain echo signal of the medium.

The time domain waveform of the radar contains a lot of information, and we will obtain the height information of the radar and the echo amplitude from the time domain waveform in subsequent research. Therefore, the inverse Fourier transform was used to transform $G^0_{xx,s}(\omega)$ into the time domain, and the time domain echo signal was expressed as $x_s(t)$:

$$x_s(t) = s(t) + e(t), \tag{14}$$

where $x_s(t)$ represents the time domain echo signal of the radar, $s(t)$ represents the reflected echo signal on the surface of the medium, and $e(t)$ represents other reflected echo signals in the environment.

After the time-domain form of the measured Green's function had been completed, the processing of the measured signal was over. The ultimate goal of this section is to obtain the echo amplitude reflected by the surface of the medium, so we extracted the peak-to-peak value of the time-domain echo signal $x_s(t)$ and expressed it as

$$A_s = \max(x_s(t)) - \min(x_s(t)), \tag{15}$$

where $\max(\cdot)$ and $\min(\cdot)$ represent the maximum value and the minimum value, respectively.

According to the basic principle of estimating the permittivity by the echo amplitude method, it is necessary to obtain both the measured echo and the total reflected echo at the same distance. It can be seen from Equation (3) that we need to know the distance between the radar and the reflection interface in advance. In this section, we present how we obtained the measured time domain echo, $x^0_s(t)$, after compensation. According to the law of phase change when electromagnetic waves propagate in a multilayer medium, the phase of the reflected echo from the air to the surface of the medium should be flipped [34]. Observing the direct waves of the system, we found that the echo at the antenna mouth surface was a positive phase and that the phase of the reflective surface echo was negative. Therefore, we extracted the time corresponding to its negative peak and took it as the time when the radar signal reaches the reflective surface, expressed as t_p. According to the time of arrival of the obtained radar signal, we could obtain the distance between the radar and the reflective surface of the medium, denoted as

$$h_p = \frac{1}{2} c t_p, \tag{16}$$

where c is the propagation speed of electromagnetic waves in the air.

2.2.2. Total Reflection Echoes Inversion

Using distance h_p, obtained in Section 2.1.1, we applied it to Equation (3) to obtain the Green's function of the total reflected echo at this distance, expressed as $G^0_{xx,m}(\omega)$, which was used as the frequency domain echo signal of total reflection and its time domain form as $x_m(t)$.

We then obtained the amplitude of the total reflection echo; that is, we could extract the peak-to-peak value of the total reflection time domain echo signal:

$$A_m = \max(x_m(t)) - \min(x_m(t)), \tag{17}$$

where $\max(\cdot)$ and $\min(\cdot)$ represent the maximum value and the minimum value, respectively.

2.2.3. Permittivity Estimation

The reflection coefficient was calculated according to amplitude values A_s and A_m of the above two echoes, and then we used the relationship between the reflection coefficient and the permittivity to obtain the estimated permittivity of the measured medium.

$$\varepsilon = \left(\frac{1+\gamma}{1-\gamma}\right)^2, \tag{18}$$

$$\gamma = \frac{A_s}{A_m}, \tag{19}$$

where γ is the reflectance coefficient.

For the multi-channel data measured by radar at one time, the change of permittivity of the wall surface on a continuous measurement line could be obtained by processing each data point separately by using the above-proposed method.

3. Experiment

To evaluate the feasibility of the proposed method, we used the SFGPR system to collect the wall surface reflection data, and we estimated the permittivity value of the wall surface of known thickness by using the method proposed in Section 2. At the same time, we carried out the wall penetration experiment and the dielectric probe detection experiment to calculate the average permittivity of the wall, and we compared it with the estimated value to prove the accuracy and precision of the proposed method. In addition, we performed a probing experiment on an adobe sample of a known height, and the permittivity estimation method introduced in Section 2 was also used to obtain an estimate of the permittivity on the sample surface, which was used to illustrate the generalization ability of the method.

3.1. Wall Permittivity Estimation Experiment

As shown in Figure 8, the radar system was placed horizontally on the sliding guide frame; the antenna port was facing the wall, and the measurement line was slid horizontally 1 m to collect the reflected signal from the wall.

Figure 8. Experimental scene.

We selected one of these data points for analysis, and its time-domain reflected echo is shown in Figure 9, which also shows the measured waveform of the antenna placed about 28 cm in front of the wall. It can be seen that the waveform before 2.5 ns was the direct wave of the system and the reflection of the antenna mouth surface, that the waveform near 3.5 ns was the reflected signal of the wall, that near 6 ns was the reflected signal of the back wall caused by electromagnetic waves penetrating the wall, that the waveform

between 3.5 ns and 6 ns may be a reflection of the internal structure of the wall, and that the waveform after 7 ns was the tailing and other reflected signals behind the wall. According to the method described in Section 2.2, the measured waveform after compensation could be obtained by removing the direct wave and compensating for the zero point of time, as shown in Figure 10.

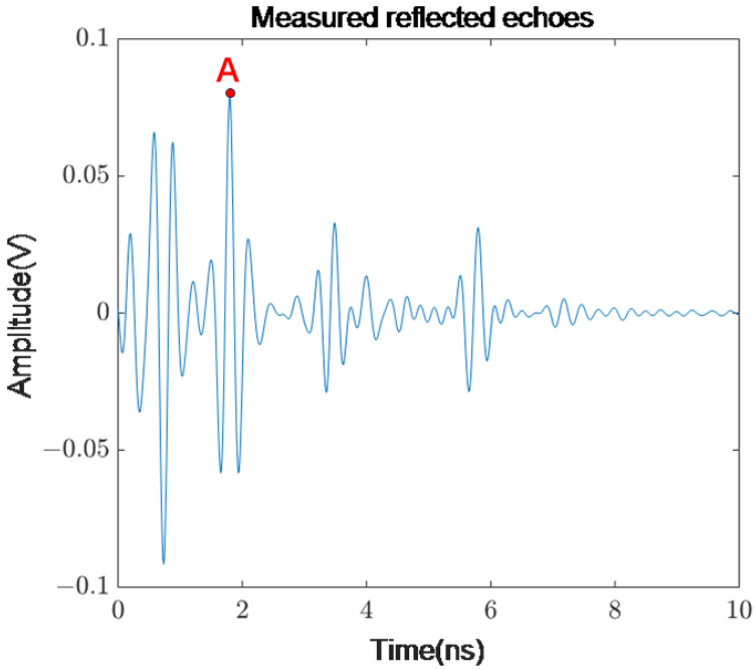

Figure 9. Measured reflection echo of wall in time domain. (Point A indicates the point where the electromagnetic wave reaches the antenna port.)

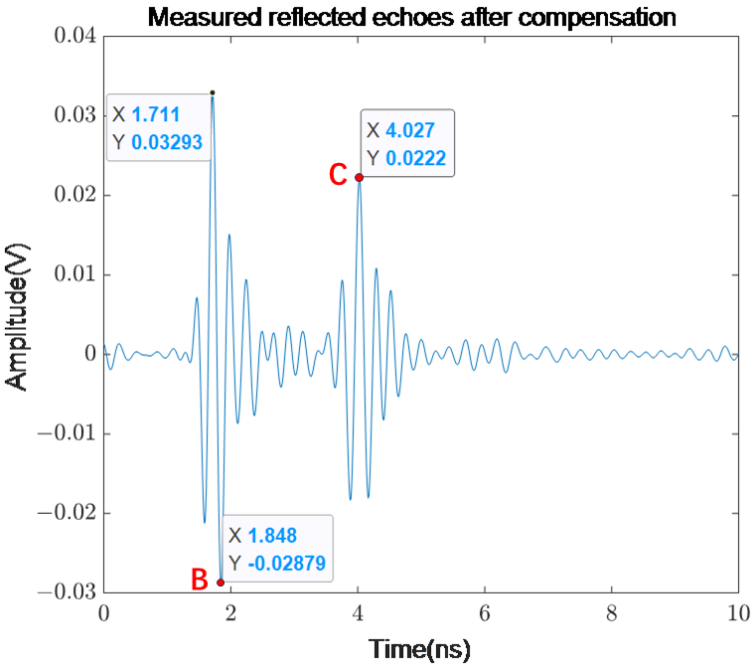

Figure 10. Measured reflection echo of the wall in time domain after compensation. (Point B indicates the point where the electromagnetic wave reaches the first wall; Point C indicates the point where the electromagnetic wave reaches the back wall.)

According to the electromagnetic law of electromagnetic waves in the propagation process, when electromagnetic waves enter vertically from one medium to another medium,

if the wave is shot by the wave-thin medium to the wave-dense medium, the reflected electromagnetic wave has a half-wave loss and additional phase difference [34]. That is, the reflected wave and the incident wave are inverted, but the transmitted electromagnetic wave has no phase change. If the electromagnetic wave is emitted from the wave-dense medium to the wave-thin medium, no phase change occurs between the reflected wave and the transmitted wave. Therefore, the first reflected echo of the electromagnetic wave on the wall is inverted with respect to the transmitted signal, and the reflected echo of the back wall is the same as the transmitted signal. It can be seen that the signal at the antenna port surface was a positive phase, which can be seen at point A in Figure 9; therefore, the first wall-reflected echo was a negative phase, which can be seen at point B in Figure 10, and then the reflected echo of the back wall was a positive phase,which can be seen at point C in Figure 10.

Thus, the first reflected echo arrival time of the wall was 1.848 ns, and the distance between the antenna and the wall could be calculated as 27.72 cm, consistent with the actual measurement. At the same time, we could also obtain the amplitude of the measured echo (i.e., extract the peak-to-peak value of its time domain signal):

$$A_s = 0.03293 - (-0.02879) = 0.06172. \tag{20}$$

After obtaining the distance from the antenna to the wall, we imported the distance and system parameters into Equation (3) to invert the total reflected echo signal at this distance, as shown in Figure 11.

The amplitude of the fully reflected echo signal could be extracted from the waveform shown in Figure 11.

$$A_m = 0.129 - (-0.1278) = 0.2568. \tag{21}$$

Substituting A_s and A_m into Equations (18) and (19) yielded an estimated permittivity of 2.66 for the wall at this scan point.

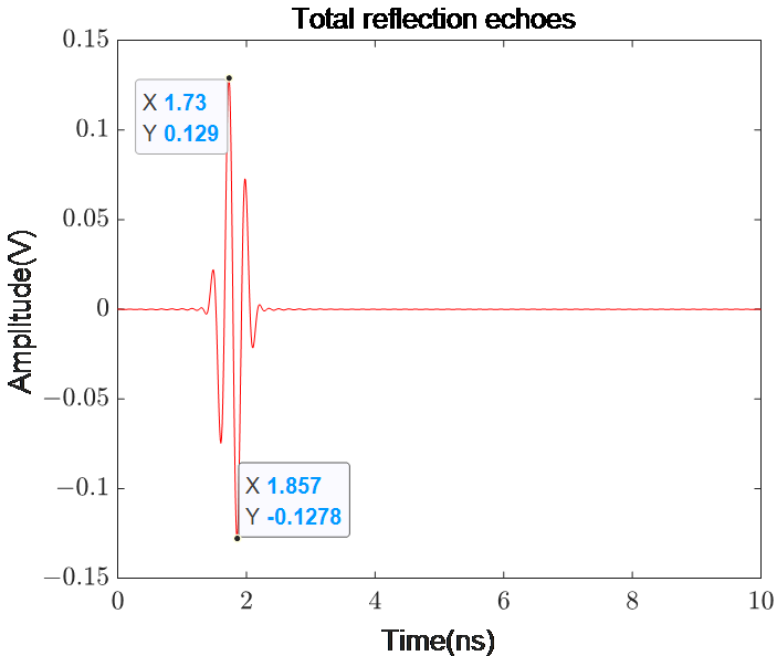

Figure 11. Total reflection echo.

From Figure 10, it can be seen that the time difference between the front surface echo and the rear surface echo of the radar lateral scan was Δt = 4.027 ns − 1.848 ns = 2.179 ns. The actual thickness of the wall was l = 19 cm, and the average permittivity of the wall at the scanning point was calculated as 2.96. The estimated permittivity differed by 0.25 from the calculated average permittivity, with a relative error of 8.4%. The former was an

estimate of the permittivity of the wall surface, and the latter was the average permittivity value of the entire wall; owing to the uneven internal structure of the wall, a certain degree of difference existed between the two.

By inverting the total reflected echoes of each sweep separately and estimating the permittivity value, we could obtain the change in the estimated permittivity on the scan measurement line, as shown in Figure 12.

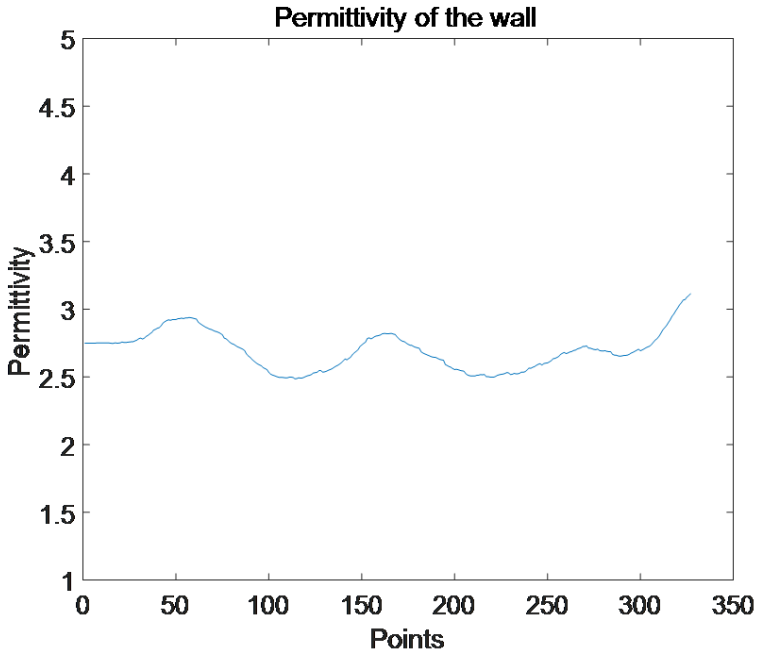

Figure 12. The change of the dielectric constant of the wall on the measuring line.

It can be seen from the change of permittivity on the measuring line that the value basically fluctuated between 2.5 and 3 and that the estimated permittivity changed relatively smoothly, with an average estimated value of 2.70. The computational cost of processing this lab process using an Intel Core i5 processor was 3.917133 s.

3.2. Verification Experiment

After using the proposed method to obtain the permittivity estimation of the wall, we verified the accuracy of the proposed method through two experiments: the wall penetration experiment and the dielectric probe detection experiment.

3.2.1. Wall Penetration Experiments

On the same wall, we used two horn antennas for the wall penetration experiments, as shown in Figure 13. The two antennas faced each other, and the distance between the two remained constant, detecting separately in the case of opposite air and penetration through the wall. According to the echo delay in the two cases and the thickness of the wall, we could obtain the average permittivity of the wall by measuring the actual thickness of the wall, and we found that it was l = 19 cm.

Owing to the difference in the permittivity of air and the wall, in the two cases above, the time difference of the received echo is denoted as

$$\frac{l}{v} - \frac{l}{c} = \Delta t, \tag{22}$$

$$v = \frac{c}{\sqrt{\varepsilon_r}}. \tag{23}$$

(**a**) (**b**)

Figure 13. Penetration experiment scene: (**a**) The two antennas were placed opposite each other. (**b**) Two antennas penetrated the wall.

Thus, according to Equations (22) and (23), the average permittivity of the wall can be denoted as

$$\varepsilon_r = \left(\frac{c \cdot \Delta t}{l} + 1\right)^2, \tag{24}$$

where v and c are the propagation speed of electromagnetic waves in the wall and air, respectively; Δt is the delay of the echo through the wall relative to the airborne echo; l is the actual thickness of the wall; and ε_r is the calculated average permittivity of the wall.

Case 1: The distance between the two antennas was 90 cm. The received echo pair in both the space-relative and wall-penetrating cases is shown in Figure 14.

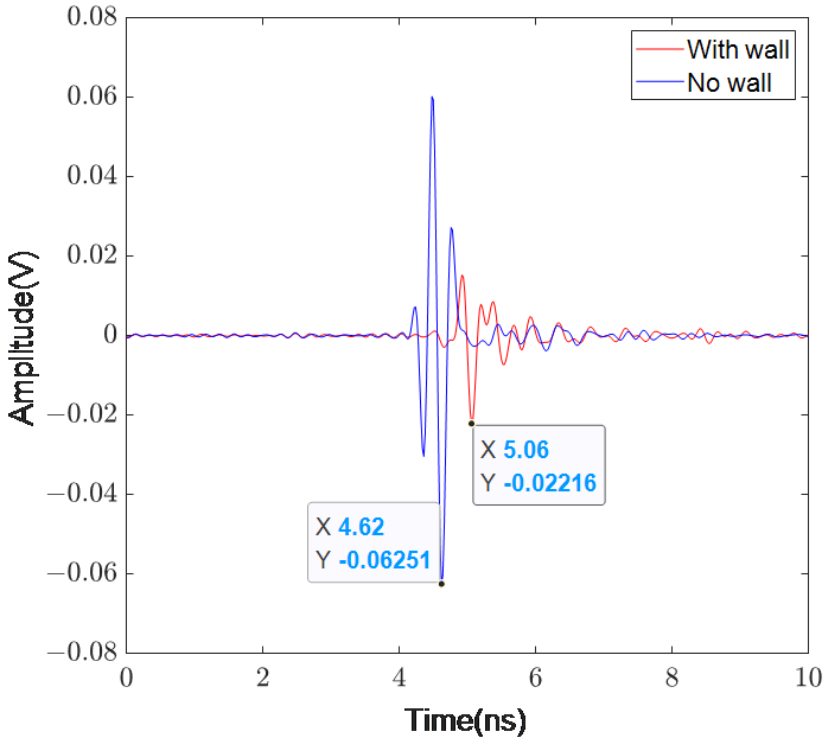

Figure 14. Comparison of received echoes when two antennas are 90 cm apart.

According to the two echoes, it can be obtained that the echo delay after penetrating the wall was comparable to that of air detection.

$$\Delta t = t_2 - t_1 = 5.06 \text{ ns} - 4.62 \text{ ns} = 0.44 \text{ ns}. \tag{25}$$

Therefore, the average permittivity of the wall could be calculated as

$$\varepsilon_r = \left(\frac{c \cdot \Delta t}{l} + 1\right)^2 = \left(\frac{3 \times 10^8 \text{ m/s} \cdot 0.44 \text{ ns}}{19 \text{ cm}} + 1\right)^2 \approx 2.87. \tag{26}$$

Case 2: The distance between the two antennas was 110 cm. The received echo pair in both the space-relative and wall-penetrating cases is shown in Figure 15.

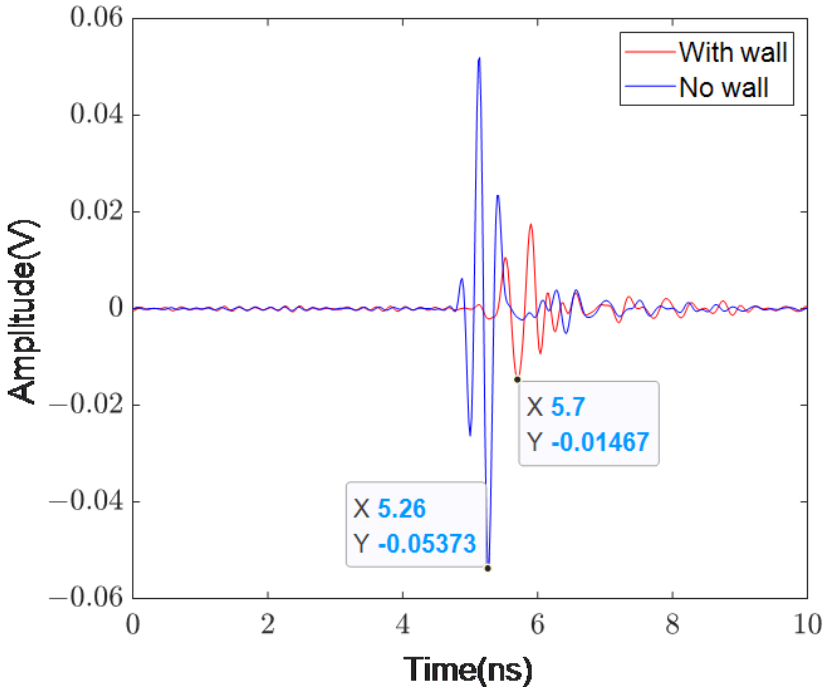

Figure 15. Comparison of received echoes when two antennas are 110 cm apart.

According to the two echoes, it can be obtained that the echo delay after penetrating the wall was comparable to that of air detection:

$$\Delta t = t_2 - t_1 = 5.7 \text{ ns} - 5.26 \text{ ns} = 0.44 \text{ ns}. \tag{27}$$

Therefore, the average permittivity of the wall could be calculated as

$$\varepsilon_r = \left(\frac{c \cdot \Delta t}{l} + 1\right)^2 = \left(\frac{3 \times 10^8 \text{ m/s} \cdot 0.44 \text{ ns}}{19 \text{ cm}} + 1\right)^2 \approx 2.87. \tag{28}$$

In two experiments at different distances, the delay of the waveform was consistent, both being 0.44 ns. Based on this delay, we could calculate the permittivity of the wall, which had a value of 2.87. Based on the experimental results, the average permittivity obtained by the antenna penetrating the wall was 2.87, the estimated permittivity of the wall was 2.70 with the method provided in Section 2.2 of this paper, and the error of the latter relative to the former was 5.9%.

3.2.2. Dielectric Probe Verification Experiment

Typically, the coaxial probe method is used to determine the relative permittivity and dielectric loss of solid or liquid high-loss electrical materials in the band from high frequencies to microwave levels [35]. This technology is popular owing to the commercial availability of related monitoring instruments and similar products in a wide frequency band [36]. The entire system is based on a network analyzer that measures the response of the material to RF or microwave energy, and the probe sends a signal to the medium under testing [37].

Five sets of experiments were performed using the Agilent 85070E dielectric probe instrument, and the probe detection scenario is shown in Figure 16.

Figure 16. Experimental scene of dielectric probe detection.

The dielectric probe test results are shown in Table 1.

Table 1. Dielectric probe test results.

Number of Experiments	Mean Dielectric Constant
1	2.8262
2	2.9186
3	2.7523
4	2.8194
5	2.6524
Mean	2.7938

Based on the analysis of experimental results, the average permittivity of the wall measured with the dielectric probe was 2.7938, and the permittivity of the wall was 2.70 according to the proposed estimation method, whose error with the former was 3.4%.

3.3. Application Experiment

In this experiment, we used a 30 cm × 30 cm × 30 cm square soil sample, which was placed above a metal plate. The experimental setup is shown in Figure 17. The sample was placed below the radar. The radar moved horizontally, and the electromagnetic waves moved vertically downward to detect along the vertical cut profile of the sample.

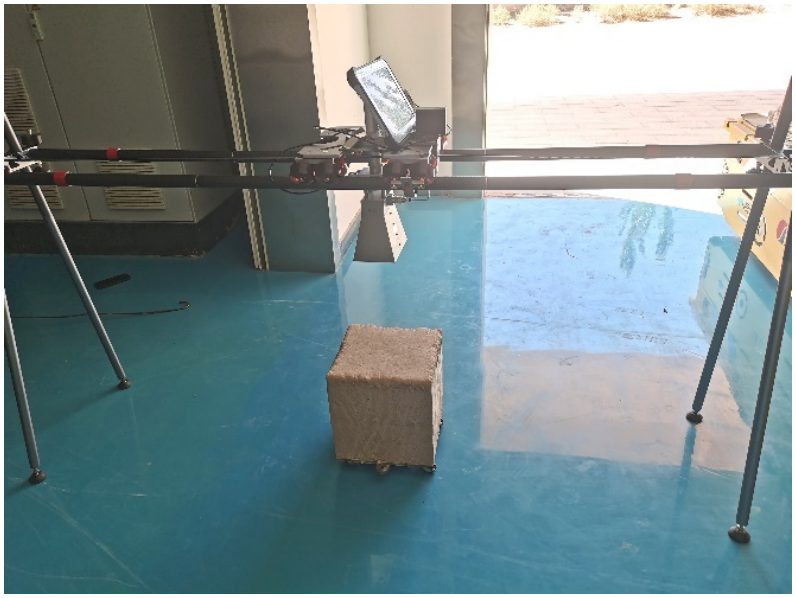

Figure 17. Experimental scene.

During the scanning process, the radar moved from one end of the sliding rail sup-port rod to the other end, the scanning distance was about 1.2 m, and the sample with a length of 30 cm was roughly located in the center of the scanning line, accounting for a quarter of the length of the measuring line. Considering the influence of the sample edge effect, to more accurately explain the characteristics of the sample, we analyzed the characteristics within one-third of the sample center. So, according to the number of sampling data channels, we intercepted roughly 50 data channels in the middle of the data for permittivity analysis. According to the full-wave inversion permittivity estimation method proposed in Section 2.2 of this paper, we could obtain the change of the estimated permittivity in the central part of the sample, which is shown in Figure 18.

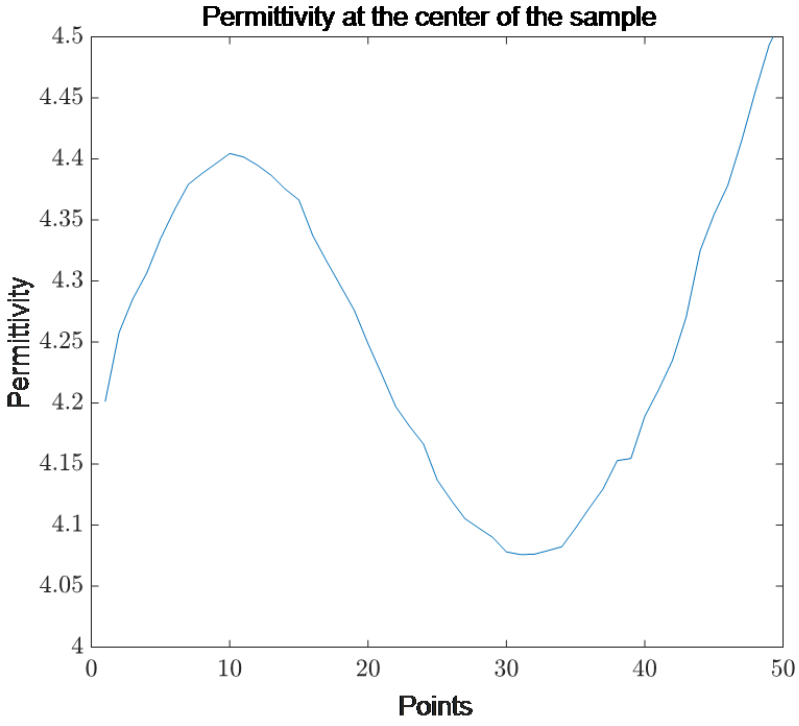

Figure 18. Permittivity at the center of the sample.

From the change in the permittivity of the sample center surface shown in Figure 18, it can be seen that the permittivity fluctuated in a small range and that the average permittivity of the sample surface was calculated to be $\varepsilon = 4.22$.

Figure 19 shows the single A-scan waveform of the sample after the compensation treatment; the reflected echo of the upper surface layer of the sample was near 2 ns, the strong reflection echo of the bottom metal plate was near 6.5 ns, and other reflections were inside the sample between the two reflections. The time difference between the two reflections was Δt = 6.266 ns − 2.258 ns = 4.008 ns. According to the actual height of the sample, 30 cm, we could calculate the average permittivity of the sample as a whole at 4.02, which is 0.2 less than the estimated value. Thus, the two are basically close. The relative error was 4.74%, which is within the acceptable range. The computational cost of processing this lab process using an Intel Core i5 processor was 4.773957 s.

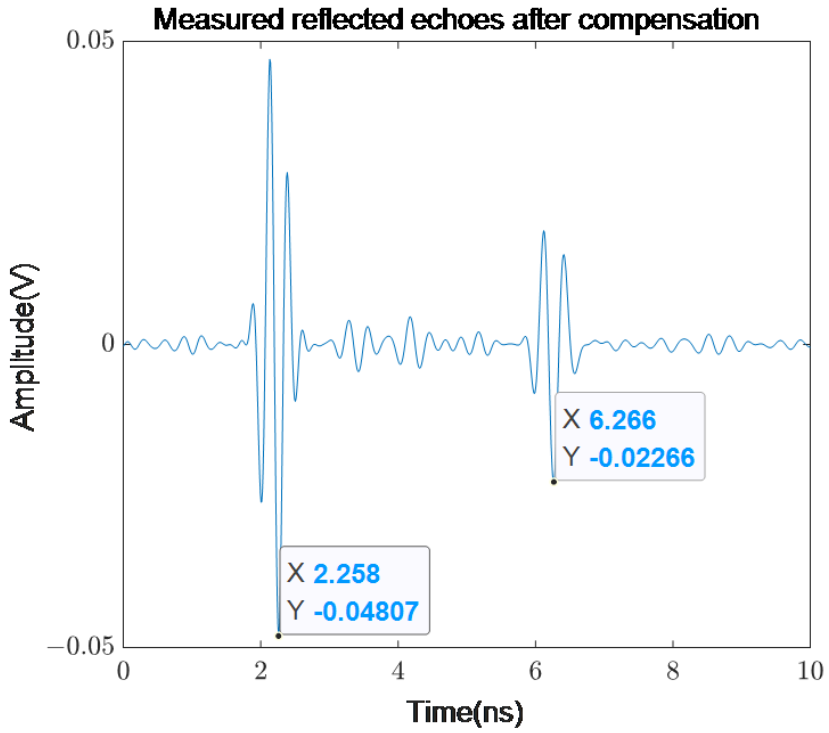

Figure 19. The reflected echo signal of the sample after compensation.

In addition, we also performed other homogeneous sample detection experiments, and the estimated results are basically consistent with the verification results. The results are shown in Table 2.

Table 2. Analysis of sample permittivity results.

Sample Serial Number	Measured Permittivity	Permittivity Verification	Relative Error
1	4.48	4.14	8.21%
2	4.05	4.06	0.25%
3	4.18	4.02	3.98%
4	4.08	4.21	3.09%
5	4.37	4.04	8.17%

Note: set measured permittivity = M; permittivity verification = N; relative error = abs(M − N)/N.

4. Discussion

The experimental results in Section 3 confirm the feasibility and accuracy of the full-wave inversion permittivity estimation method proposed in this paper.

In a real scenario, a wall that can be passed through can often be manually measured for its thickness, and the radar system used can penetrate the wall to obtain reflections from the back wall. So, according to the actual thickness of the wall and the time difference between the reflected waves of the front and rear walls, it is easy to calculate the average permittivity value of the wall, which can be used as a reference for the estimation results of the proposed method. We also could obtain the change of the estimated permittivity of the wall on a measurement line. In the wall detection experiment, the average permittivity of the wall was 2.96, the estimated permittivity obtained by the full-wave inversion method was 2.70, and the error between the two was 8.8%. The estimated permittivity was the value of the wall surface, and since the inside of the wall must be uneven, the error between the two was within the acceptable range. The estimated permittivity on this measurement line basically fluctuated between 2.5 and 3, and the change was relatively stable.

In the wall penetration experiment, we used two antennas to calculate the average permittivity of the wall by observing the difference between the relative space and the arrival time difference of the receiving wave through the wall. We analyzed the cases at two distances, and the average permittivity calculated in both cases was 2.87, with a relative error of 5.9% from the estimate. The dielectric probe is a simple and intuitive permittivity detection instrument. Using the probe to test the wall many times, we found that the average value of the permittivity was 2.7938 and that the relative error between it and the estimated value was 3.4%. The error between the above two verification experimental results and the results obtained by the proposed method was within a controllable range.

Finally, we used an adobe model of a known height as an experimental object, which was placed above the metal plate. The estimated permittivity using the full-wave inversion method was 4.22, while the average permittivity of the sample was 4.02 based on the time difference between the reflected wave of the upper surface and the metal plate. The permittivity obtained by the two methods was relatively close, with an error of 4.74%.

The above experimental results confirm the feasibility of the full-wave inversion permittivity estimation method proposed in this paper and indicate that the method has high accuracy and generalization ability.

5. Conclusions

The full-wave inversion real-time permittivity estimation method for SFGPR proposed in this paper has a simple estimation process and high calculation accuracy. The built radar system can efficiently remove direct waves and clutter (e.g., multiple reflections), and it can accurately compensate for the zero time-point of the signal. The total reflection waveform at different distances can be obtained by inversion, without the need to carry out cumbersome metal plate calibration experiments. Also, it is easy to obtain the permittivity estimate on a continuous measurement line, which can solve estimation needs under the amount of large data, greatly reduce the workload and improve work efficiency. Moreover, this method is suitable for penetrating radars such as through-wall radar and GPR, and it has a wide range of applicable scenarios, which can solve the permittivity estimation requirements of most media. Thus, the method can provide a basis for grasping the condition of the measured medium, which can ensure the accuracy of detection and improve the subsequent data processing efficiency.

Author Contributions: Conceptualization, X.L. (Xu Li), S.Y. and Q.K.; methodology, X.L. (Xu Li) and S.Y.; software, X.L. (Xu Li), S.Y. and C.S.; validation, X.L. (Xu Li), S.Y. and Q.K.; formal analysis, X.L. (Xu Li) and X.L. (Xiaojun Liu); investigation, G.F. and X.L. (Xiaojun Liu); resources, G.F. and S.Y.; data curation, G.F., S.Y. and C.S.; writing—original draft preparation, X.L. (Xu Li); writing—review and editing, S.Y. and C.S.; visualization, X.L. (Xiaojun Liu); supervision, G.F.; project administration, X.L. (Xiaojun Liu) and S.Y.; funding acquisition, S.Y. and G.F. All authors have read and agreed to the published version of the manuscript.

Funding: This research was funded by the Strategic Priority Research Program of the Chinese Academy of Sciences, grant number XDA28050302, and by Science and Technology on Near-Surface Detection Laboratory, grant number 6142414220710.

Data Availability Statement: Not applicable.

Conflicts of Interest: The authors declare no conflict of interest.

References

1. Yang, X.; Kruk, J.v.; Bikowski, J.; Kumbhar, P.; Vereecken, H.; Meles, G.A. Full-waveform inversion of GPR data in frequency-domain. In Proceedings of the 2012 14th International Conference on Ground Penetrating Radar (GPR), Shanghai, China, 4–8 June 2012; pp. 324–328. [CrossRef]
2. Kopeikin, V.V.; Morozov, P.A.; Edemskiy, F.D.; Edemskiy, D.E.; Pavlovskii, B.R.; Sungurov, Y.A. Experience of GPR application in oil-and-gas industry. In Proceedings of the 2012 14th International Conference on Ground Penetrating Radar (GPR), Shanghai, China, 4–8 June 2012; pp. 811–815. [CrossRef]
3. Zhou, L.; Su, Y. GPR Imaging With RM Algorithm in Layered Mediums. *IEEE Geosci. Remote Sens. Lett.* **2011**, *8*, 934–938. [CrossRef]
4. Ni, Z.-K.; Shi, C.; Pan, J.; Zheng, Z.; Ye, S.; Fang, G. Declutter-GAN: GPR B-Scan Data Clutter Removal Using Conditional Generative Adversarial Nets. *IEEE Geosci. Remote Sens. Lett.* **2022**, *19*, 4023105. [CrossRef]
5. Kovalenko, V.; Yarovoy, A.G.; Ligthart, L.P. A Novel Clutter Suppression Algorithm for Landmine Detection With GPR. *IEEE Trans. Geosci. Remote Sens.* **2007**, *45*, 3740–3751. [CrossRef]
6. Feng, X.; Sato, M.; Liu, C. Subsurface Imaging Using a Handheld GPR MD System, *IEEE Geosci. Remote Sens. Lett.* **2012**, *9*, 659–662. [CrossRef]
7. Benedetto, A.; Tosti, F.; Ciampoli, L.B.; Pajewski, L.; Pirrone, D.; Umiliaco, A.; Brancadoro, M.G. A simulation-based approach for railway applications using GPR. In Proceedings of the 2016 16th International Conference on Ground Penetrating Radar (GPR), Hong Kong, China, 13–16 June 2016; pp. 1–6. [CrossRef]
8. Bilik, Y.; Haridim, M.; Bilik, D. Reflectivity and Resolution Improvement of Underground Rectilinear Objects Detection Using GPR. *IEEE Geosci. Remote Sens. Lett.* **2020**, *17*, 799–803. [CrossRef]
9. Sato, M. GPR for disaster mitigation and beyond. In Proceedings of the 2012 14th International Conference on Ground Penetrating Radar (GPR), Shanghai, China, 4–8 June 2012; pp. 17–20. [CrossRef]
10. Fernández, M.G.; López, Y.Á; Arboleya, A.A.; Valdés, B.G.; Vaqueiro, Y.R.; Andrés, F.L.H.; García, A.P. Synthetic Aperture Radar Imaging System for Landmine Detection Using a Ground Penetrating Radar on Board a Un-manned Aerial Vehicle. *IEEE Access* **2018**, *6*, 45100–45112. [CrossRef]
11. Garcia-Fernandez, M.; Alvarez-Lopez, Y.; Gonzalez-Valdes, B.; Rodriguez-Vaqueiro, Y.; Arboleya-Arboleya, A.; Heras, F.L. Recent advances in high-resolution Ground Penetrating Radar on board an Unmanned Aerial Vehicle. In Proceedings of the 2019 13th European Conference on Antennas and Propagation (EuCAP), Krakow, Poland, 31 March–5 April 2019; pp. 1–5.
12. Fernández, M.G.; Narciandi, G.Á.; Arboleya, A.; Antuña, C.V.; Andrés, F.L.-H.; López, Y.Á. Development of an Airborne-Based GPR System for Landmine and IED Detection: Antenna Analysis and Intercomparison. *IEEE Access* **2021**, *9*, 127382–127396. [CrossRef]
13. Tronca, G.; Tsalicoalou, I.; Lehner, S.; Catanzariti, G. Comparison of pulsed and stepped frequency continuous wave (SFCW) GPR systems. In Proceedings of the 2018 17th International Conference on Ground Penetrating Radar (GPR), Rapperswil, Switzerland, 18–21 June 2018; pp. 1–4. [CrossRef]
14. Hamran, S.E.; Gjessing, D.T.; Hjelmstad, J.; Aarholt, E. Ground penetrating synthetic pulse radar: Dynamic range and modes of operation. *J. Appl. Geophys.* **1995**, *33*, 7–14. [CrossRef]
15. Schantz, H.G. Dispersion and UWB antennas. In Proceedings of the 2004 International Workshop on Ultra Wideband Systems Joint with Conference on Ultra Wideband Systems and Technologies, Joint UWBST & IWUWBS 2004 (IEEE Cat. No.04EX812), Kyoto, Japan, 18–21 May 2004; pp. 161–165. [CrossRef]
16. Zhang, J.; Ye, S.; Yi, L.; Lin, Y.; Liu, H.; Fang, G. A Hybrid Method Applied to Improve the Efficiency of Full-Waveform Inversion for Pavement Characteriza-tion. *Sensors* **2018**, *18*, 2916. [CrossRef] [PubMed]
17. Lambot, S.; Slob, E.C.; Bosch, I.v.; Stockbroeckx, B.; Vanclooster, M. Modeling of ground-penetrating Radar for accurate characterization of subsurface electric properties. *IEEE Trans. Geosci. Remote Sens.* **2004**, *42*, 2555–2568. [CrossRef]
18. Zhang, J.W.; Ye, S.B.; Guo, R.J.; Liu, X.F.; Fang, G.Y. A Novel Forward Model of Ground Penetrating Radar In The Far Field. In Proceedings of the 2018 17th International Conference on Ground Penetrating Radar (GPR), Rapperswil, Switzerland, 18–21 June 2018; pp. 1–6. [CrossRef]
19. Zhang, J.; Ye, S.; Lin, Y.; Liu, X.; Fang, G. A Modified Model for Quasi-Monostatic Ground Penetrating Radar. *IEEE Geosci. Remote Sens. Lett.* **2020**, *17*, 406–410. [CrossRef]
20. Lambot, S.; Slob, E.C.; Bosch, I.v.; Stockbroeckx, B.; Scheers, B.; Vanclooster, M. GPR design and modeling for identifying the shallow subsurface dielectric properties. In Proceedings of the 2nd International Workshop onAdvanced Ground Penetrating Radar, Delft, The Netherlands, 14–16 May 2003; pp. 130–135. [CrossRef]
21. Rohman, B.P.A.; Nishimoto, M. Concrete Dielectric Constant Estimation Based on Analytic Signal Peak Ratio of GPR Response for Non-Destructive Inspec-tion. In Proceedings of the IGARSS 2019–2019 IEEE International Geoscience and Remote Sensing Symposium, Yokohama, Japan, 28 July–2 August 2019; pp. 6376–6379. [CrossRef]

22. Fereidoony, F.; Chamaani, S.; Sebt, M.A.; Mirtaheri, S.A. Efficient method for estimation of the thicknesses and complex dielectric constant of wall. In Proceedings of the 8th European Conference on Antennas and Propagation (EuCAP 2014), The Hague, The Netherlands, 6–11 April 2014; pp. 3085–3088. [CrossRef]
23. Loulizi, A. Development of Ground Penetrating Radar Signal Modeling and Implementation for Transportation Infrastructure. Ph.D. Thesis, Virginia Tech, Blacksburg, VA, USA, 2001.
24. Klotzsche, A.; Jonard, F.; Looms, M.C.; van der Kruk, J.; Huisman, J.A. Measuring Soil Water Content with Ground Penetrating Radar: A Decade of Progress. *Vadose Zone J.* **2018**, *17*, 180052. [CrossRef]
25. Busch, S.; van der Kruk, J.; Vereecken, H. Improved Characterization of Fine-Texture Soils Using On-Ground GPR Full-Waveform Inversion. *IEEE Trans. Geosci. Remote Sens.* **2014**, *52*, 3947–3958. [CrossRef]
26. Zhang, Y.; Zhou, Y.; Feng, T.; Gao, Y.; Li, E.; Zhou, J. A Method for Determining Vector Reflection Coefficient Based on Scalar Amplitude. *IEEE Antennas Wirel. Propag. Lett.* **2020**, *19*, 497–501. [CrossRef]
27. Giannopoulos, A.; Diamanti, N. A numerical investigation into the accuracy of determining dielectric properties and thicknesses of pavement layers using reflection amplitude GPR data. In Proceedings of the Tenth International Conference on Grounds Penetrating Radar, GPR 2004, Delft, The Netherlands, 21–24 June 2004; pp. 655–658.
28. Virieux, J.; Operto, S. An overview of full-waveform inversion in exploration geophysics. *Geophysics* **2009**, *74*, WCC1–WCC26. [CrossRef]
29. Watson, F.; Lionheart, W. SVD analysis of GPR full-wave inversion. In Proceedings of the 15th International Conference on Ground Penetrating Radar, Brussels, Belgium, 30 June–4 July 2014; pp. 484–490.
30. Klotzsche, A.; Vereecken, H.; van der Kruk, J. GPR full-waveform inversion of a variably saturated soil-aquifer system. *J. Appl. Geophys.* **2019**, *170*, 103823. [CrossRef]
31. da Silva, S.L.E.F.; Karsou, A.; de Souza, A.; Capuzzo, F.; Costa, F.; Moreira, R.; Cetale, M. A graph-space optimal transport objective function based on q-statistics to mitigate cycle-skipping issues in FWI. *Geophys. J. Int.* **2022**, *231*, 1363–1385. [CrossRef]
32. Karanth, A.; Onkar, N.; Smitha, N.S.N.; Sridhara; Singh, V. Through-wall imaging system using horn antennas. In Proceedings of the 2017 4th International Conference on Advanced Computing and Communication Systems (ICACCS), Coimbatore, India, 6–7 January 2017; pp. 1–6. [CrossRef]
33. Mosig, J. The Weighted Averages Algorithm Revisited. *IEEE Trans. Antennas Propag.* **2012**, *60*, 2011–2018. [CrossRef]
34. Maosheng, C.; Jie, Y.; Haitao, L.; Xiaoyong, F.; Jing, Z. A simulation of the quasi-standing wave and generalized half-wave loss of electromagnetic wave in non-ideal media. *Mater. Des.* **2003**, *24*, 31–35. [CrossRef]
35. Shibata, K.; Kobayashi, M. Numerical Calculation Error of Variational Method with Dielectric Measurement Using a Coaxial-probe. In Proceedings of the 2018 IEEE International RF and Microwave Conference (RFM), Penang, Malaysia, 17–19 December 2018; pp. 223–226. [CrossRef]
36. Shibata, K.; Kobayashi, M. Property Measurement Errors Based on Application of an Estimation Equation Using the Coaxial Probe Method. In Proceedings of the 2019 IEEE MTT-S International Microwave and RF Conference (IMARC), Mumbai, India, 13–15 December 2019; pp. 1–5. [CrossRef]
37. Karim, M.N.A.; Malek, M.F.A.; Jamlos, M.F. Permittivity measurement of different types of soil for ground penetrating radar applications, In Proceedings of the 2014 2nd International Conference on Electronic Design (ICED), Penang, Malaysia, 19–21 August 2014; pp. 479–482. [CrossRef]